



An ultra-wideband compact design for hyperthermia: Open ridged-waveguide antenna

Downloaded from: <https://research.chalmers.se>, 2022-07-02 09:47 UTC

Citation for the original published paper (version of record):

Ghaderi Aram, M., Aliakbarian, H., Dobsicek Trefna, H. (2022). An ultra-wideband compact design for hyperthermia: Open ridged-waveguide antenna. *IET Microwaves, Antennas and Propagation*, 16(2-3): 137-152. <http://dx.doi.org/10.1049/mia2.12226>

N.B. When citing this work, cite the original published paper.

An ultra-wideband compact design for hyperthermia: Open ridged-waveguide antenna

Morteza Ghaderi Aram¹  | Hadi Aliakbarian² | Hana Dobšiček Trefná¹

¹Department of Electrical Engineering, Chalmers University of Technology, Gothenburg, Sweden

²K. N. Toosi University of Technology, Tehran, Iran

Correspondence

Morteza Ghaderi Aram, Gibraltargatan 88, 412 79, Gothenburg, Sweden.

Email: aramg@chalmers.se

Abstract

Antennas are the building block of radiative hyperthermia (HT) applicators. This study proposes a compact UWB antenna specifically tailored to meet the requirements for deep HT array applicators. The proposed Open Ridged-Waveguide (ORWG) antenna, which is an adaptation of a double-ridged horn antenna, operates over the frequency band of 400–800 MHz. It was experimentally assessed as a single element. The quality metrics considered were reflection coefficient, penetration depth, effective field size (EFS), and mutual coupling. The design shows a 75.5% fractional bandwidth with a reflection coefficient measured to be below -10 dB from 367 up to 820 MHz. The EFS is greater than the physical dimensions of the 3-by-4 cm aperture. The mutual coupling between two adjacent elements in the array, measured in a flat phantom arrangement, is lower than -30 dB throughout the entire band. The antenna's performance was further tested in two deep HT scenarios in order to assess the mutual coupling and focussing abilities while in the array configuration. To this end, phased array applicators consisting of 10 and 16 ORWG antennas were simulated in CST, and the results are presented for a homogeneous cylindrical muscle phantom and a realistic patient model, respectively. The good agreement between the simulated and measured results suggests that the antenna can be successfully used for HT.

KEYWORDS

biomedical antennas, double-ridged horn antennas, hyperthermia, specific absorption rate (SAR), UWB antennas

1 | INTRODUCTION

Defined as the induced temperature rise up to 40–44°C, hyperthermia (HT) has been shown to improve the therapeutic outcome of the conventional cancer treatment modalities such as radiotherapy and chemotherapy [1–5]. In microwave (MW) HT, the electromagnetic (EM) energy is administered to the body using applicators. To achieve an appropriate penetration, these applicators use antennas that mainly operate in the lower part of the UHF band. Antennas are placed around the patient typically in an annular phased array configuration [6]. Localised heating in the tumour is achieved through the positive wave interference mechanism. In other words, by applying different amplitudes and phases at the feeding points of the antennas,

the focal point can be steered in order to target the tumour. The antenna element design is the cornerstone of HT devices and must fulfil multiple requirements. In general, the desired attributes of antennas, used in HT, are small dimensions, a highly directional and symmetrical pattern with a reflection coefficient better than -10 dB, low mutual coupling, and power handling capability of at least 150 W [7, 8]. A broader operational bandwidth is also advantageous because it gives the opportunity to modulate the size of the focal spot.

Hyperthermia applicators are loaded by a patient typically located in the near field of the antenna. Moreover, the presence of a matching medium, which often has the form of a water-filled plastic bag and is known as water bolus, is essential. This is because the placement of the water bolus between the

This is an open access article under the terms of the Creative Commons Attribution License, which permits use, distribution and reproduction in any medium, provided the original work is properly cited.

© 2022 The Authors. *IET Microwaves, Antennas & Propagation* published by John Wiley & Sons Ltd on behalf of The Institution of Engineering and Technology.

antenna and the body further facilitates the transmission of the field into the patient's body and prevents heating of the body surface [9, 10]. The design procedure of such a loaded antenna is clearly different from the antenna designs operating in free space. The design characteristics and conventional verification procedures widely used in the antenna and propagation society, such as far-field radiation pattern, gain, or efficiency are therefore not applicable due to the propagation in lossy media [11, 12]. Penetration depth and power deposition pattern defined in terms of effective field size (EFS) and depth [13, 14] are instead viable measures to appraise the efficacy of the antennas designed for HT applicators.

Despite a variety of antenna types proposed for phased array configurations, only some of them have reached the clinical utilisation as reviewed recently [6]. The applicators based on dipoles [15], hollow waveguides [16, 17], and microstrip patch antennas [18, 19] have demonstrated their efficiency and applicability in treatment of tumours in pelvic and head and neck (H&N) regions. Nevertheless, none of these systems were designed for a wide-band operation, and having narrowband antenna elements limits their flexibility to target the thermal dose into tumours of different volumes. Their inherently narrowband characteristic poses a challenge in further development of heating devices that are capable of modifying the size of the focal spot.

In an attempt to extend the bandwidth limitations, different adaptations of bow-tie antennas have been recently proposed [20–22]. In particular, the self-grounded bow-tie (SGBW) antenna [21] is a UWB design that allows for MR thermometry, thanks to its suitable magnetic field distribution. Such a design [22] paves the way towards having a dual modality system of MR thermometry during HT treatments [23]. The main drawback of the bow-tie antennas, however, is the necessity of using a balun. Acting as an RF-matching network, the balun ensures a symmetric radiation field and stable electrical performance throughout the operation band [24]. Apart from enlarging the dimensions, adding to the complexity, and decreasing the efficiency due to power absorption in the structure, the matching networks often pose challenges in terms of the mutual coupling and EM compatibility (EMC) [25]. Therefore, in terms of reliability and reproducibility, antennas where an RF matching network can be avoided have a clear advantage when used for clinical trials. Making RF transceivers less susceptible to the environmental noise, the avoidance of baluns has also an impact on the final quality of the reconstructed images in MW imaging (MWI) and thermometry applications [12, 26].

Waveguide [16] and horn antennas [27] are preferable from the EMC perspective, because they are inherently shielded by their metallic housing. The metallic back structure directs the radiation forward and blocks any back radiation. Moreover, the horn's metallic walls prevent any direct coupling to the adjacent elements through the air. Their clinical implementation has been already associated with first systems due to relatively simple fabrication and excitation as well as high peak power handling capability. Conventional horn and waveguide antennas, however, have suffered from a limited bandwidth. The

need for the bandwidth extension has led to the use of ridges in the flare section of the horn antennas [28–30]. This new subset of the horn-type family is commonly referred to as the double-ridged horn (DRH) antenna, which typically consists of a back cavity and a ridged waveguide (RWG) that begins to flare close to the aperture. In fact, the capacitance effect of adding the ridges inside the waveguide increases the single mode bandwidth by lowering the cut-off frequency of the dominant propagating mode (TE_{10}) [31–33]. Propagation of higher-order modes inside the structure could however lead to undesired effects in the radiation characteristic and therefore should be avoided [34].

In this work, we propose a UWB antenna for MW HT, which originates from and further expands the concept of DRH antennas. We call the new design Open Ridged-Waveguide (ORWG) antenna whose fundamental principles are described in Section 2. The ORWG antenna exhibits a wide bandwidth achieved without needing any balun or RF-matching network. Moreover, due to its metallic housing, it is inherently shielded and therefore less susceptible to the crosstalk or to the environmental noise and interference in general. The performance of the antenna was assessed in terms of procedures prescribed by European Society for Hyperthermic Oncology (ESHO) Quality Assurance guidelines [13]. Additional metrics were also used to assess the near-field directivity (NFD) and power deposition capabilities. Furthermore, the robustness of the design against the variations in the arrangement typical for HT was assessed. Finally, the antenna's potential to act as an element in phased array systems was numerically assessed in setups with a homogeneous phantom and a realistic patient model. The setups and evaluation metrics are presented in Section 3 while the performance is reported in Section 4. Section 5 provides some concluding remarks.

2 | ANTENNA DESIGN

Using closed-form expressions for RWG structures [35], in this section, we first show the procedure of scaling a well-established horn design [36] to the desired frequency band in UHF. Then the design is further tailored for hyperthermic applications and used as a starting point for a rigorous optimisation.

2.1 | Design of the DRH antenna in air

The initial design was inspired by a UWB DRH antenna proposed for radar and EMC applications in the X and Ku bands (8–18 GHz) [36]. In order to shift the centre frequency from 13 GHz to 500 MHz, the outer dimensions of the back cavity, waveguide, and the flare parts were up-scaled by a factor of $SF = 13 \text{ GHz}/500 \text{ MHz} = 26$.

For the ridge parts inside the metallic frame, an exponential taper of the coaxial feed line ($z_0 = 50 \Omega$) to the impedance of free space ($\eta_0 = 377 \Omega$) is considered as follows:

$$Z(z) = Z_0 e^{kz} \quad (1)$$

where $k = \frac{1}{L} \ln\left(\frac{Z_0}{Z_L}\right)$ for the specified length of L . The length of the taper is then divided into equidistant segments in the z -direction. The impedance of each segment, given by Equation (1), dictates a certain profile height of the ridge in the corresponding segment, which can be calculated from the following closed-form expression of ridged-waveguides [35]:

$$Z(z) = \frac{Z_{0\infty}}{\sqrt{1 - (\lambda/\lambda_{cr})^2}} \quad (2)$$

where λ is the wavelength and

$$Z_{0\infty} = \frac{120\pi^2(b/\lambda_{cr})}{\frac{b}{s} \sin\pi \frac{W}{b} \frac{b}{\lambda_{cr}} + \left[\frac{B_0}{Y_0} + \tan\pi \frac{b}{\lambda_{cr}} \frac{(a-W)}{2b}\right] \cos\pi \frac{W}{b} \frac{b}{\lambda_{cr}}} \quad (3)$$

$$\frac{b}{\lambda_{cr}} = \frac{b}{2(a-W)} \left[1 + \frac{4}{\pi} \left(1 + 0.2 \sqrt{\frac{b}{a-W}} \right) \times \right. \quad (4)$$

$$\left. \frac{b}{a-W} \ln\left(\csc\left(\frac{\pi s}{2b}\right)\right) + \left(2.45 + 0.2 \frac{W}{a}\right) \frac{Wb}{s(a-w)} \right]^{-\frac{1}{2}},$$

$$\frac{B_0}{Y_0} \cong \frac{2b}{\lambda_{cr}} \ln\left(\csc\left(\frac{\pi d}{2b}\right)\right) \quad (5)$$

and parameters a , b , W , and s are according to Figure 1a. The exponential tapering of the physical profile is then found using $\frac{S_0}{2} e^{\tau z}$ with factor τ coming from a simple curve fitting to the segments and should not be confused with the exponential impedance tapering k introduced earlier. Finally, the resultant profile is shown in Figure 1b, with the blue curve showing the physical taper and the red curve representing the impedance taper. As can be seen, half of the gap between the tapered ridges starts with 1 cm at the feed location where the line impedance is 50 Ω and ends up with 16 cm at the aperture where we have the intrinsic impedance of free space.

2.2 | Tailoring the DRH design for hyperthermia applicators

As shown in Figure 1a, the dimensions of the scaled DRH antenna are $a = 473.2$ mm, $b = 150.8$ mm, and $L = 794.8$ mm. Note that the longitudinal dimension, that is L , is particularly larger than the other dimensions because according to Ref. [37], the prolongation of the flare section can result in higher gains. Overall, the air-filled horn design is too big to be feasible for biomedical applications. Furthermore, it has not yet been loaded by a lossy medium in front of the aperture. The performance in terms of the reflection coefficient (the blue dashed line in Figure 2) is, however,

favourable to be a good starting point for a hyperthermic design. An effective and common way to reduce the dimensions of the structure is to fill it with water [38, 39]. High ϵ_r of water provides a down-scaling factor of $\sqrt{\epsilon_{rw}} \approx 9$ for both the antenna size as well as for impedances at both ends of the tapered profile.

On the other hand, since water is a lossy medium, its presence inside the horn leads to undesirable power losses inside the structure. This power loss works also against the above-mentioned design principle, which associates higher gain to a longer flare section. Therefore, the flare section was abandoned in the new design. This compact, water-filled version of the original design is no longer a conventional horn antenna. Thus, no closed-form or explicit expression for its impedance is available.

2.3 | Design of the loaded water-filled ORWG antenna

The shortened antenna of the previous section with flat ridges does not exhibit the desired S_{11} characteristic as shown in Figure 2 (red dashed line). To improve the impedance matching, tapering was applied on the ridges situated across the waveguide section. To further increase the degree of freedom for impedance matching between both ends of the profile, the width of the ridges was released to change along the transverse axis (controlled by the factor W_Factor in Table 1). The built-in particle swarm optimisation (PSO) of the CST MW Studio [40] was used to fine-tune the parameters. The resulting design was called the ORWG antenna and it is visualised in Figure 3a. All the details about the geometry are shown in Figure 4, and the parameters used for optimization along with their upper and lower limits are tabulated in Table 1. The reflection coefficient S_{11} of the optimised design, depicted by the solid black line in Figure 2, fulfils the bandwidth requirements.

3 | MATERIALS AND METHODS

The aperture of the fabricated ORWG antenna was covered by a thin, rubber diaphragm as shown in Figure 3b. Experimental verification was performed in a standardised setup with a muscle tissue load as described by ESHO Quality Assurance guidelines [13, 14]. Furthermore, we utilised an additional metric to assess the NFD, which allows for a comparison with other designs. Finally, we assessed the robustness of the design against the variations in the arrangement typical in HT.

Figure 5 depicts the arrangement used for both design and verification procedures. A single antenna element was attached to a surface water bolus with the thickness of 30 mm placed on top of a homogeneous slab of a muscle tissue phantom with dimensions $360 \times 250 \times 60$ mm. In the

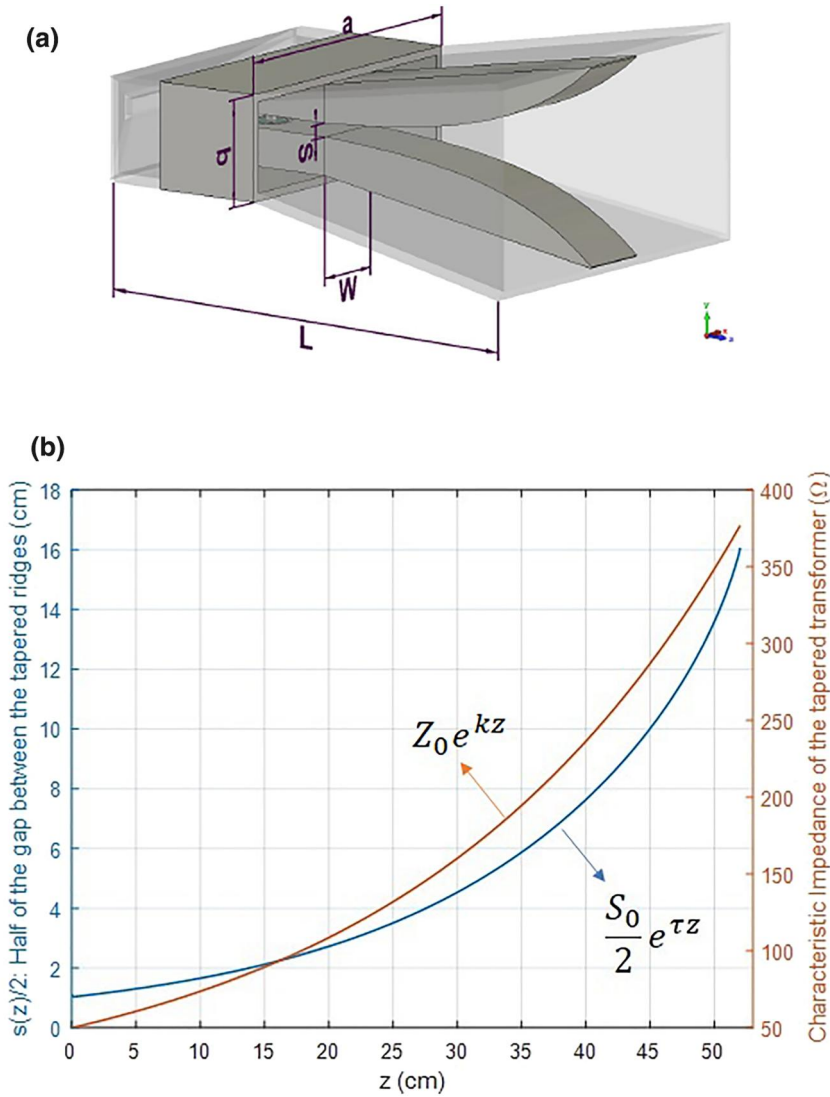


FIGURE 1 (a) Scaled double-ridged horn (DRH) design for the UHF band in air with transparent flares and back cavity (b) Tapered profile along with the exponential impedance matching from 50Ω to that of free space (377Ω)

design stage, using the CST MW Studio as the full-wave EM solver, the deionised water was modelled based on the dispersive Debye model, while the dielectric properties of the muscle were calculated using the Cole–Cole dispersion model [41]. In the verification phase, a hydrogel water bolus [42], which is a convenient solution to replace water-filled plastic bags in HT procedures, was used. The relative permittivities, assessed using the Agilent 85070E dielectric probe kit, were constant throughout the examined frequency band and they read as 78 and 60 for hydrogel and muscle phantom, respectively. Their conductivities increased with frequency and were measured to be in the range of $[0.3\text{--}0.5]$ and $[0.4\text{--}0.9]$, respectively.

3.1 | Numerical assessment of the power deposition patterns

Efficient power deposition is one of the fundamental attributes of an HT antenna. In this sense, we examined the capability of

the ORWG antenna in terms of power deposition in the target tissue, NFD, and near-field radiation pattern. Moreover, we compared its performance against the SGBW antenna of Ref. [21]. Currently, various adaptations of this design [22] provide the highest bandwidth along with a directive radiation pattern. Both designs were simulated under the same condition for the standard setup of Figure 5a.

The NFD, as proposed by Ref. [43], is a metric that shows the proportion of the power radiated via the front aperture. It considers a cuboid enclosing the antenna. The radiated power over the front surface (P_f) as well as the total radiated power over the entire cuboid's surface (P_t) are computed as the flux integral of the real part of the Poynting vector over the respective surfaces. Near-field directivity is then given as the following ratio $\text{NFD} = P_f/P_t$.

The near-field radiation patterns based on the power flow of each design were calculated in the principal E- and H-planes along the circular scan lines with a fixed radius of 60 mm. This radius represents one wavelength in water at the centre frequency; see Figure 11 for details.

FIGURE 2 Simulated S_{11} of the double-ridged horn (DRH) design under the free-space propagation condition along with the reflection coefficient of the initial cut-version with flat ridges and the optimised one having tapered ridges

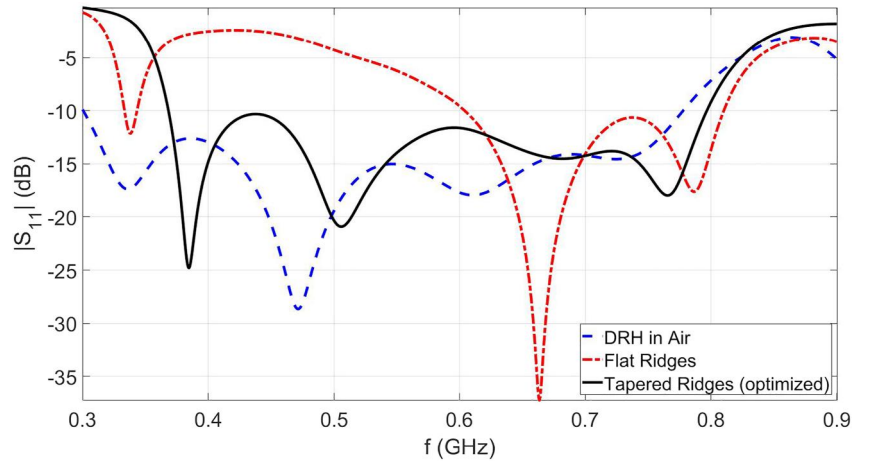


TABLE 1 Upper and lower limits as well as optimised values of the parameters shown in Figures 1 and 4

Parameters	Lower limit	Upper limit	Optimised
a	31.6	53.5	37.2
b	16.3	35.6	30.9
W	27.9	37.7	32.8
s_0	6.2	12.4	9.3
BackCavLen1	2.4	3.2	2.8
BackCavLen2	3.9	5.4	4.7
W_Factor	0.82	1.11	0.96
τ	0.019	0.027	0.023
L	19.9	26.9	23.4
OffsetFromEdge	0.21	0.28	0.24
ShortEndW	11	15	13
ShortEndL	3.2	4.3	3.7

Note: Values are all in millimetres.

3.2 | Robustness of the reflection coefficient against variations in the arrangement

As the final part of the design procedure, robustness of the reflection coefficient of the antenna against variations in water temperature, water bolus thickness, and the patient anatomy was assessed. As the antenna is expected to operate at high power of 150 W over a typically 1-h HT treatment session, the water inside the internal structure needs to be circulated through a small water inlet/outlet. Furthermore, the water temperature should be kept constant, due to thermal dependence of dielectric parameters that may notably alter the reflection coefficient of the antenna.

In annular phased array applicators, the distance of the antenna to the body varies due to the different geometry and anatomy of the treated region. The variation of the reflection coefficient with the thickness of the water bolus placed between the antenna and the body was assessed in the flat

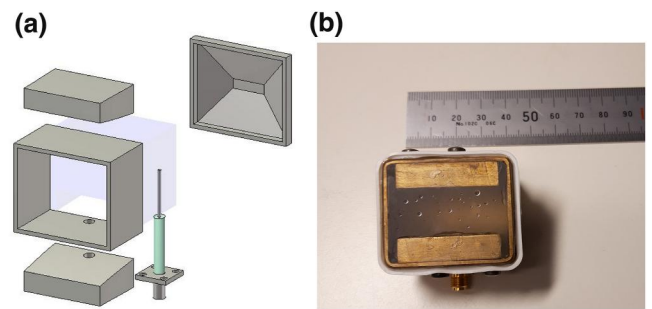


FIGURE 3 (a) The water-filled Open Ridged-Waveguide (ORWG) model and its different parts. (b) The fabricated ORWG antenna

phantom scenario. The variation of the reflection coefficient with the patient anatomy was also examined in an annular phased array setup in which the antennas were arranged in two rings, each having eight antennas as visualised in Figure 6b.

3.3 | Verification procedures

The heating ability of the antenna was assessed according to the QA guidelines for superficial HT [13, 14]. The temperature rise as well as the thermal EFS and depth were assessed. The phantom was exposed to the radiation from a single antenna for 6 min in a setup presented in Figure 5b, and the temperature was monitored at different locations by fibre optic probes (FISO Technologies) located in the phantom according to Figure 5a.

The EFS, effective penetration depth (EPD) [44], and their corresponding modern alternatives thermal EFS (TEFS) and thermal EPD (TEPD) [13] are common metrics to assess the performance of HT applicators. In particular, the procedures have been proposed for the assessment of superficial applicators, but the important characteristics of antennas employed in phased arrays can be captured as well. The EFS is defined by the area within 50% of the maximum specific absorption rate (SAR) contour in the 1 cm deep plane under the aperture. According

to the guidelines, a good radiator for superficial HT needs to have an EFS greater or at least equal to its physical aperture size so that side-by-side elements in an array configuration leave no area of the tissue surface uncovered. The EPD is defined by the depth where the SAR falls to 50% of the maximum SAR at 1 cm depth. The thermal alternatives are characterised in the same way but in terms of the achieved temperatures.

The EFS and EPD were numerically assessed for six frequencies within the operation band of the antenna, while the experimental characterisation was carried out for two frequencies in two separate occasions. In particular, the first

scenario was carried out at a frequency of 475 MHz for a 10-min long exposure with 7 W, while the second scenario assessed the operation at 600 MHz for a 6-min long exposure with 25 W.

To assess the TEFS and TEPD experimentally, the muscle phantom is precut 1 cm below its surface, and after exposure, temperature profiles are captured by an infrared camera (B355, FLIR Systems). The temperature rise achieved in a homogeneous non-perfused phantom in a defined period of time (Δt) can be directly related to the SAR as follows:

$$\Delta T \approx \frac{\text{SAR}}{c} \Delta t \quad (6)$$

where ΔT is the temperature rise and c is the heat capacity of the phantom. Finally, the experimental results in terms of TEFS and TEPD were compared.

3.4 | Cross-coupling and power deposition capability in array configurations

Full spatial coverage in annular phased array applicators is usually materialised by having several rings of antennas with a small inter-ring distance in between. To mimic the placement of antennas in such a configuration, two fabricated ORWG antennas are placed next to each other as shown in the inset of Figure 7.

As an example that is closer to H&N scenarios due to the proximity of this part of the body to a cylinder, we considered a 10-element cylindrical array simulated using the frequency domain solver of CST. The setup, shown in Figure 6a, consists of a muscle phantom, which is 120 mm in diameter and has a height of 200 mm, while the diameter and height of the water bolus are 200 mm and 120 mm, respectively.

To illustrate the potential of the antenna to deposit EM energy into a large, deep-seated, intracranial tumour, an elliptical

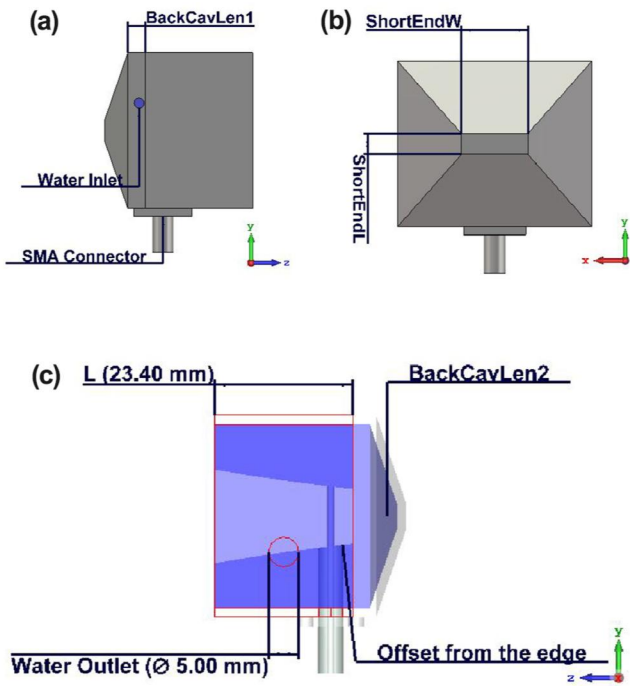


FIGURE 4 Parameters of the Open Ridged-Waveguide (ORWG) antenna, which are used in the optimisation process

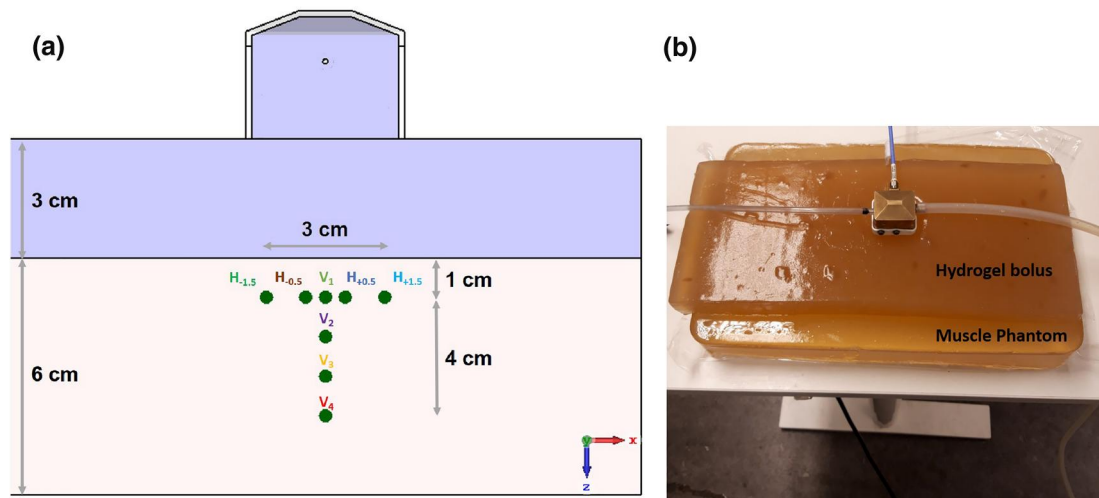


FIGURE 5 (a) Schematic illustration (b) photograph of the setup used in the design and verification procedures

array of 16 antennas was simulated in CST. The antennas were arranged in two rings, each containing eight antennas, and placed around a patient model containing the intracranial tumour, Figure 6b. A realistic patient model of a child, segmented into 10 tissue types with a high resolution ($1 \times 1 \times 1$ mm), was used. Dielectric properties of the tissues and other details about the model are given in a previous study [8]. This setup challenged the antenna to variations in the water bolus thickness as well as to the anatomical variation of the body. Finally, the antennas were excited by discrete ports at 400 MHz. The excitation amplitudes and phases were calculated using an in-house developed beam-former based on PSO, details of which are given elsewhere [45]. These parameters, optimised for the cost function of the hotspot-tumour-quotient (HTQ) [46], are then used to steer the focal point on the tumour and also to reduce the hotspots outside the targeted area.

4 | RESULTS

As shown in the inset of Figure 7, two fabricated ORWGs are placed next to each other to mimic the antenna placement in a phased array configuration. Figure 7 shows the simulated and

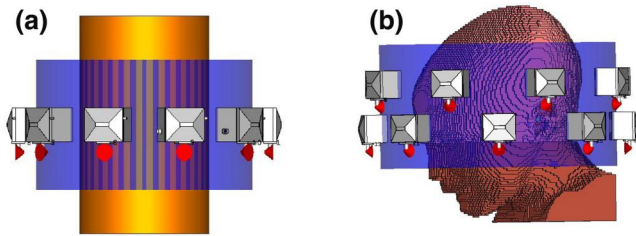


FIGURE 6 Phased array of (a) 10-element cylindrical and (b) 16-element elliptical configurations for a homogeneous muscle phantom and a realistic child model, respectively

measured S-parameters of the scenario when the first antenna is in the transmitter mode while the second acts as a receiver. As can be seen, the design exhibits a 75.5% bandwidth with $S_{11} < -10$ dB from 367 up to 820 MHz.

4.1 | Numerical assessment of the power deposition patterns

Figure 8 shows SAR patterns in the H-plane of four representative frequencies in the band, that is 400, 450, 650, and 800. They are reported for the simulated input power of 10 W. Patterns in the E-plane are similar and therefore not reported here. Although smaller in terms of the SAR-coverage, the pattern in 650 MHz shows the highest peak SAR value of 66.2 (W/kg) deposited in the muscle. The antenna thus meets one of the most important design criteria, which requires a stable radiation pattern over the entire frequency band of 400–800 MHz.

For a specific and detailed comparison, the performance of ORWG on the standard setup was compared with that of the SGBW antenna. Firstly, the amount of power deposited by both designs in the target tissue, that is muscle, is depicted in Figure 9a. These values were readily accessible from the simulations where CST separated PLDs per material type for a broadband sweep in the range of [300–800] MHz with a ten-MHz frequency step under the normalised excitation power of 0.5 W for each frequency sample. As can be seen from the figure, ORWG is more capable of depositing power in the lower part of the frequency band. The trend changes for frequencies above 600 MHz, where SGBW performs marginally better. Figure 9b shows the differential power deposited at each frequency, with the green and red shades favouring the ORWG and SGBW antennas, respectively. Subtracting the negative area below the differential curve from the positive part, we observe that ORWG deposits

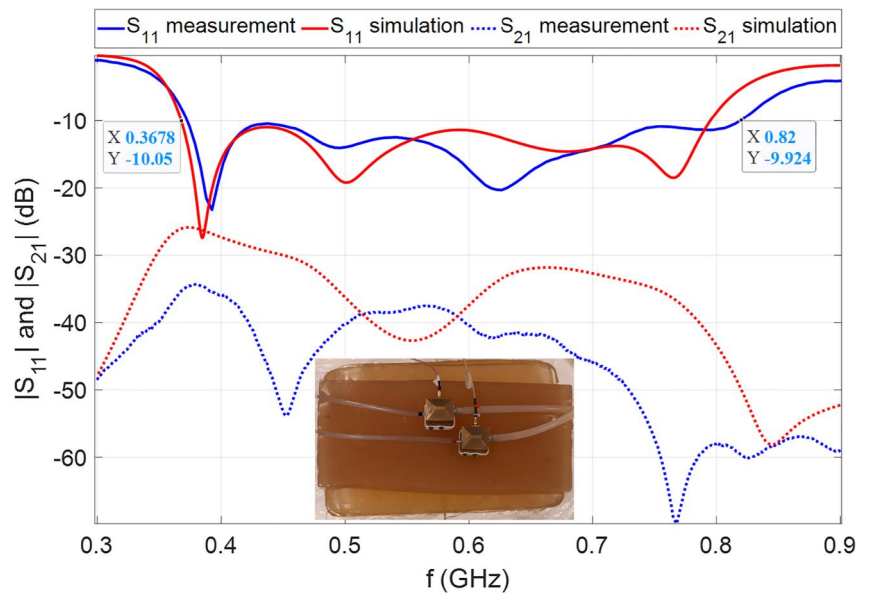


FIGURE 7 Simulated and measured S_{11} and S_{21} of the Open Ridged-Waveguide (ORWG) antennas as shown in the inset

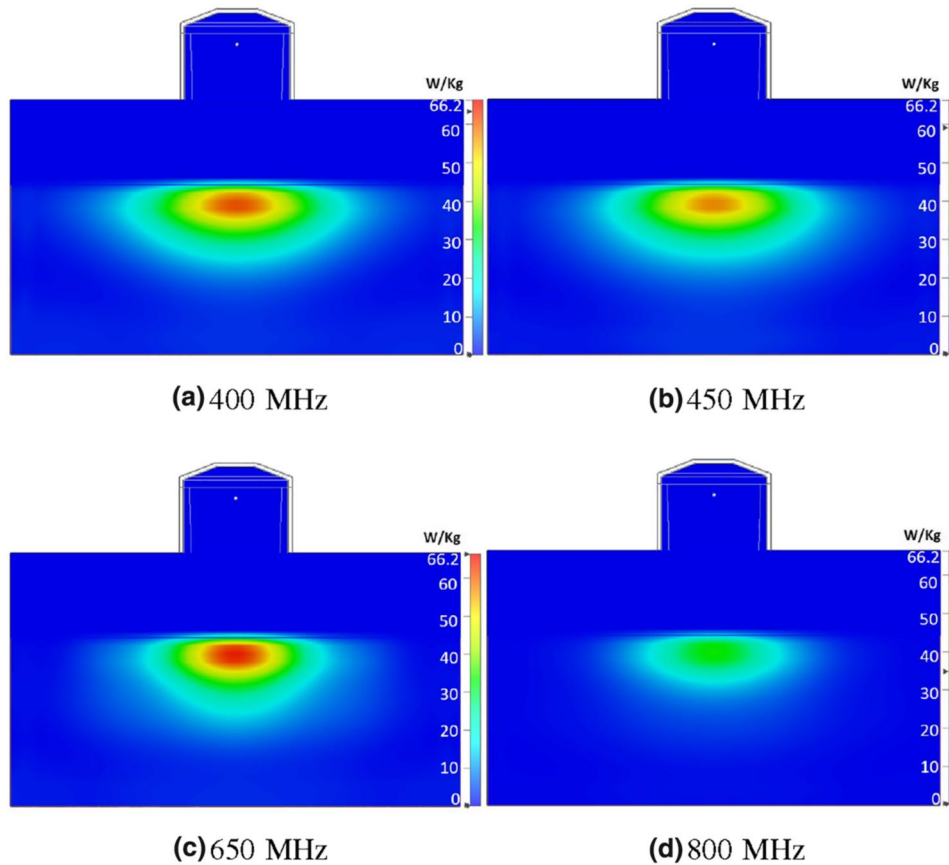


FIGURE 8 Specific absorption rate (SAR) distributions at several different frequencies in the band

1.92 W more in the target tissue throughout the whole band than SGBW.

Secondly, Figure 10 shows that the ORWG antenna couples more than 95% of the total radiated EM energy to the “outside world” through its front aperture. A comparison of the NFD factors shows that the NFD of ORWG not only surpasses that of SGBW but is also higher than the reported NFD factors for MWI antennas in both Ref. [47, 48].

Thirdly, as can be seen from the near-field radiation patterns of Figure 11, ORWG shows a stable radiation pattern with no significant back lobes. In contrast, SGBW has a considerable back lobe compared to ORWG at all frequencies reported. This comes from the presence of the balun in the design of the SGBW antenna, which reduces its radiation efficiency. Note that the power values ($A \cdot V/m^2$) reported in dB in these plots are not normalised and should not be interpreted as gain but rather as a tool that allows us to compare the general behaviour and radiation sidelobes of the two designs.

4.2 | Sensitivity analysis

Figure 12 shows variations in the measured S_{11} with respect to the temperature variation of deionised water inside the

structure. Despite small alteration in the bandwidth, the shift towards high frequencies can be observed with an increased water temperature. Furthermore, water temperature above 22°C shifts the reflection coefficient above -10 dB in the range of 450–550 MHz, which is, of course, undesirable. Therefore, the water needs to be maintained at constant temperatures below 22°C through a continuous circulation mechanism.

In annular phased array applicators, the thickness of the water bolus varies due to the natural curvature of the body under treatment. Therefore, it seems necessary to investigate the impact of this variation on the antenna's reflection coefficient. The result of the parametric sweep of water bolus thickness is reported in Figure 13 for thicknesses of 10, 20, and 30 mm. As can be seen from the figure, the lowest resonance frequency of the design increases due to a decrease in the water bolus thickness. As a result, the reflection coefficient remains below -10 dB throughout the entire band. However, the situation will certainly change if a substantial contrast in the propagation impedance of the medium occurs, an example of which can be the presence of air gaps between antenna-bolus or bolus-muscle interfaces. Good contact is therefore required. A similar rationale is valid even for a deliberate discontinuity imposed on the design by enclosing the aperture of the antenna. In

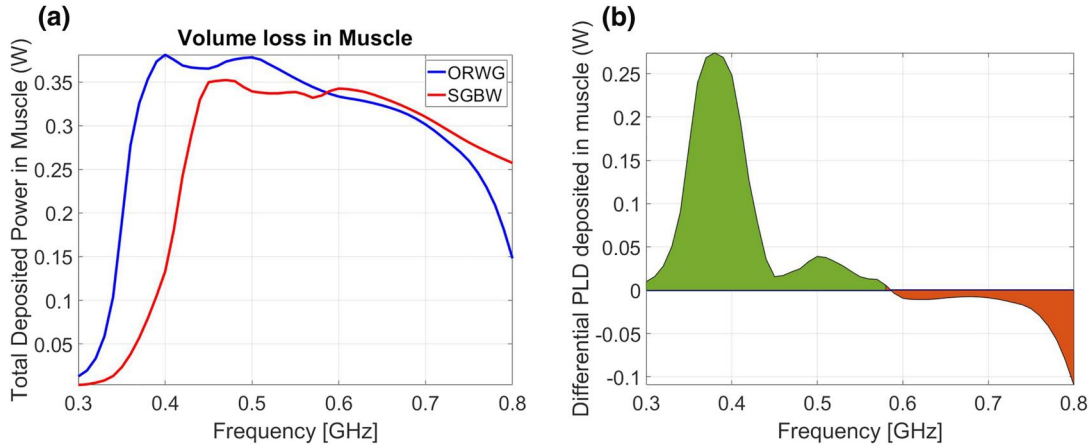


FIGURE 9 Comparison of the Open Ridged-Waveguide (ORWG) with self-grounded bow-tie (SGBW) antenna in terms of the power deposition in the target tissue

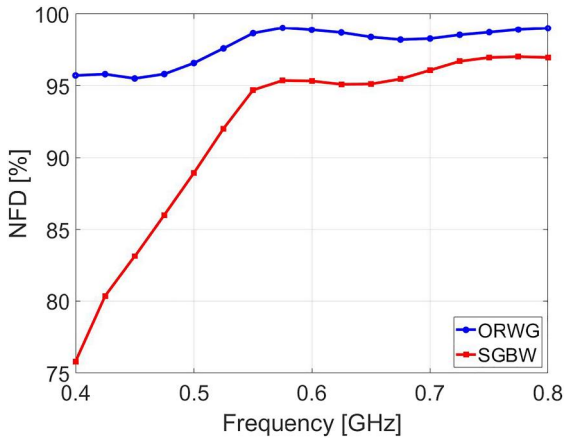


FIGURE 10 Comparison of the Open Ridged-Waveguide (ORWG) with self-grounded bow-tie (SGBW) antenna in terms of near-field directivity (NFD)

the current fabrication, we used a thin rubber membrane as the lid in front of the antenna aperture. Being thin in comparison to the wavelength, this membrane did not affect the performance of the antenna despite having a low ϵ_r of about 2. However, the use of thicker, more durable material would be more favourable under clinical circumstances. A thicker lid with higher dielectric permittivity, such as Rogers RO3010 with ϵ_r of 11, might be of interest in future studies.

The setup, shown in Figure 6b, was used to study the variation of the reflection coefficient with respect to the patient anatomy in an annular phased array configuration in which the antennas were arranged in 2 rings each having 8 antennas. As can be seen from Figure 14, the reflection coefficient of all antennas remain below -10 dB throughout the entire band. Despite small variations in the lower part of the operational band, all antennas operate at least at 400 MHz as required by the design criteria.

4.3 | Performance metrics based on hyperthermia quality assurance guidelines

4.3.1 | The simulated results

Table 2 reports the EFS and EPD for frequencies within the band. The maximum SAR at 1 cm depth in the muscle phantom is fairly constant at frequencies up to 650 MHz, where the maximum occurs, and then it starts to decrease at higher frequencies. Interestingly, the maximum EPD that barely goes beyond 1 cm is not correlated with this frequency but rather with 600 MHz.

The last column of Table 2 visually illustrates the 50% iso-SAR of EFS overlaid with the antenna aperture. This visual inspection also provides interesting information about how the radiation pattern changes from a circle at 400 to a horizontal ellipse at 500 MHz, rotates then to a vertical ellipse at 600, and finally goes back to a circle at 700 MHz. Despite small alternations in the geometrical shape, the EFS extends beyond the area of the physical aperture for almost all frequencies in the band. As both EPD and $\text{SAR}_{\text{Max}1\text{cm}}$ falls rapidly at 800 MHz, colour of the EFS changes from red to pink.

4.3.2 | Experimental verification

The ORWG design was validated at two frequencies, that is. 475 and 600 MHz, in a dedicated measurement setup shown in Figure 5. Figures 15a and 15b display the thermal EFS (TEFS) captured by an infrared camera. We initially aimed at the input power of 10 W so as to be consistent with the simulation, but then by using an RF power metre (Bird 4421 Multifunction Power Metre), we realised that the power amplifier in the lab could not provide more than 7 W at 475 MHz while it gave 25 W at 600 MHz. When it comes to the shape and pattern, the detailed heating

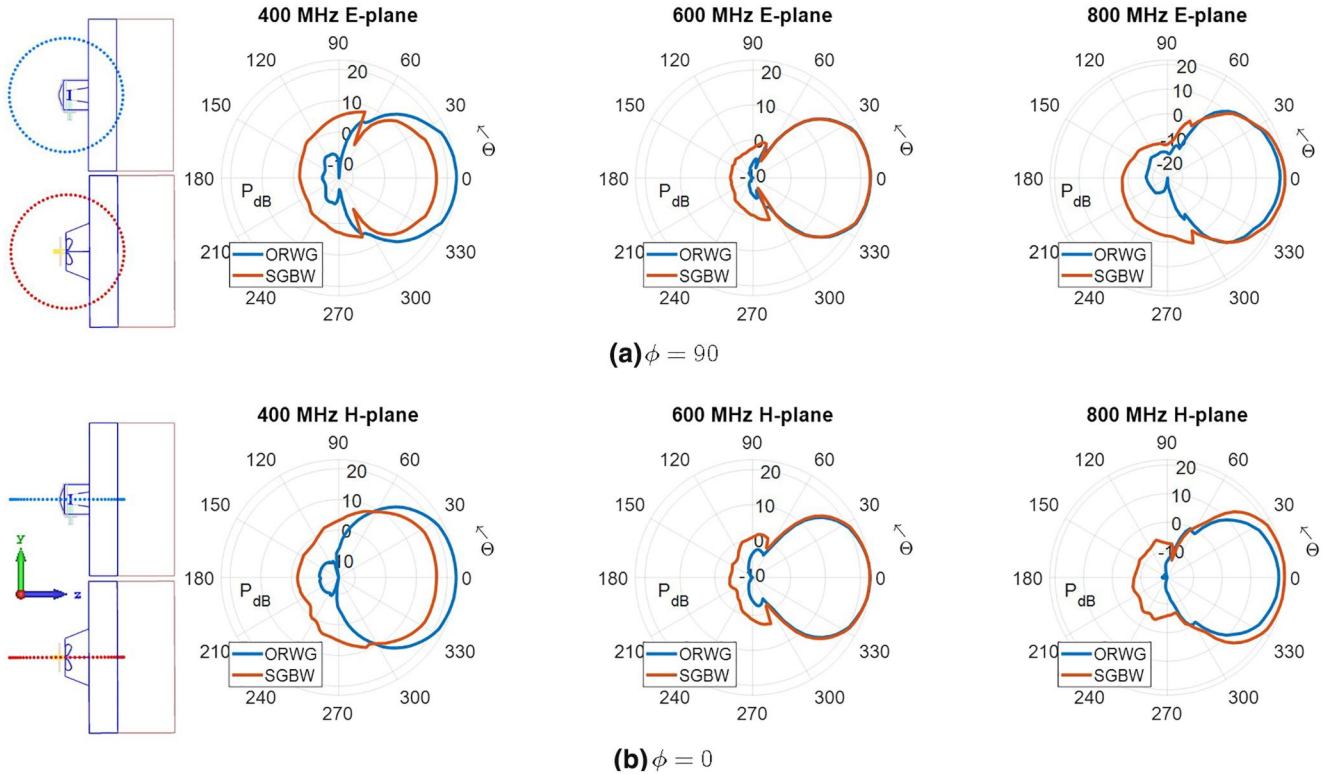


FIGURE 11 Comparison of Open Ridged-Waveguide (ORWG) with the self-grounded bow-tie (SGBW) antenna in terms of their near-field radiation patterns at 400, 600, and 800 MHz in (a) E-plane (b) H-plane

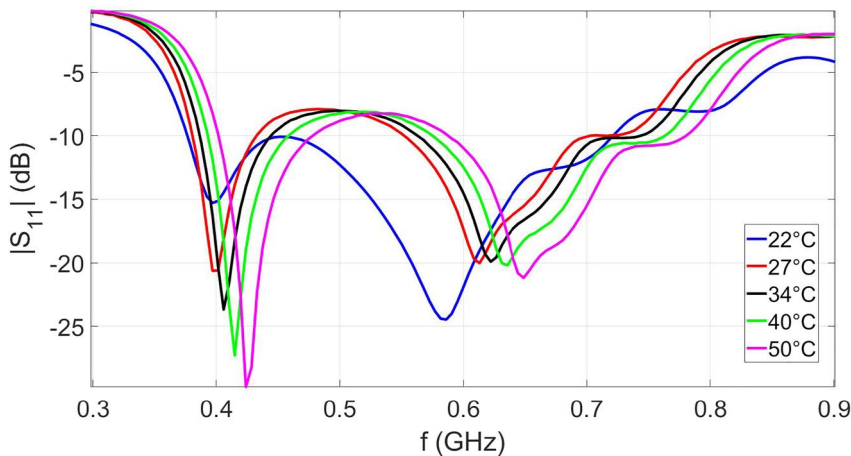


FIGURE 12 Measurements of the antenna's reflection coefficient under a heated condition to show the sensitivity of the characteristic to the temperature variation in water

patterns depicted in Figure 15c and 15d confirm the numerically predicted EFS patterns in Table 2. The maximum temperature rise achieved along the central axis of the aperture was about 6°C and 14°C for 475 and 600 MHz, respectively. The TEFS of the antenna, given by 50% isoline, has an area of 3750 and 2237 mm^2 for the respective cases.

Figure 16a visualises the temperature increase in the muscle phantom during the exposure at 600 MHz, as monitored using thermal sensors. The sensors were located both horizontally 1 cm below the phantom surface and vertically along the

antenna centre as depicted in Figure 5a. Dashed lines in Figure 16a, associated with the horizontal probes, show the symmetry of the pattern around the antenna centre, whereas the solid lines, related to the vertical probes, indicate a fast decline of the temperature at higher depth. A comparison between these experimentally achieved temperatures with the temperatures calculated for the same scenario in CST is provided in Figure 16b and 16c. In particular, the temperatures at probe locations are compared with the 2-D simulated temperature profiles at the end of the exposure, that is, after 6 min. The experimental and simulated data demonstrate similar

FIGURE 13 Parametric sweep on the thickness of the water bolus and its impact on S_{11}

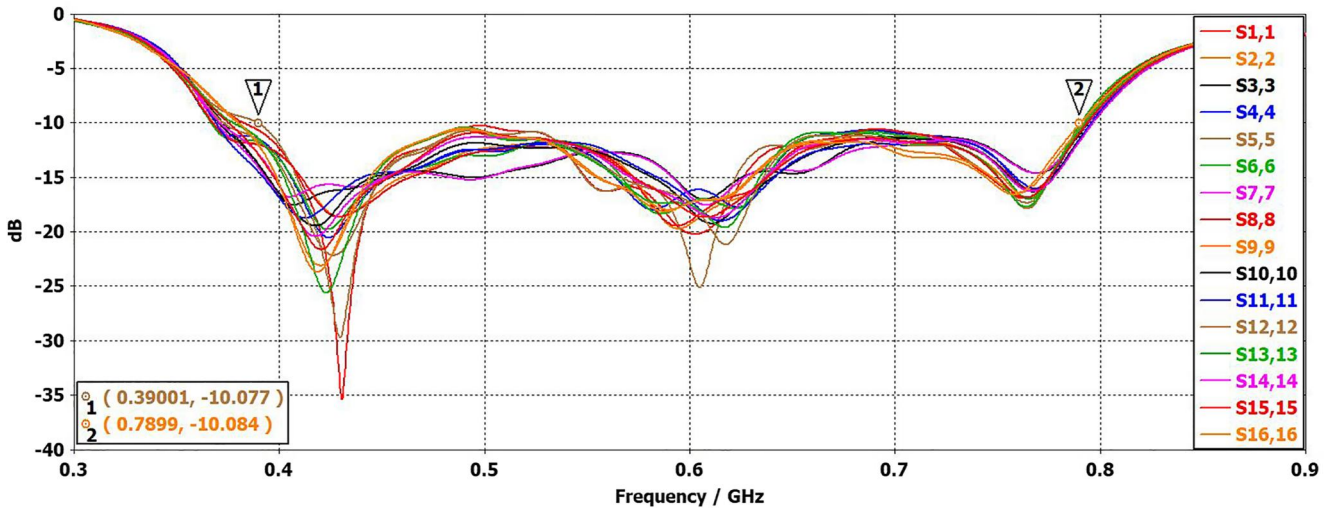
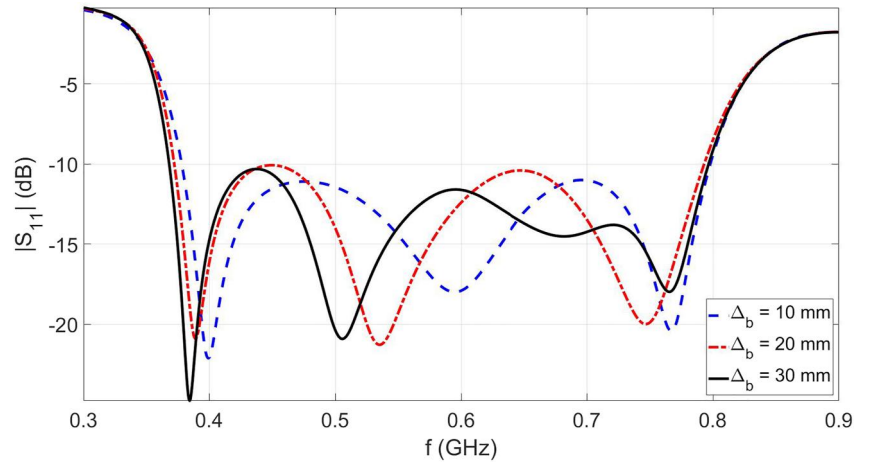


FIGURE 14 Reflection coefficient of all 16 elements having an impedance bandwidth better than -10 dB in the range of [390–790] MHz

trends. Nevertheless, the measured temperatures are at least 2° C lower than the simulated ones. This is, however, not the case for the $V_{1\text{cm}}$ sensor, which shows the same temperature as the simulation. Very likely, the tip of the probe, containing the sensor, was not placed in the depth of 1 cm but slightly above. Another justification for the lower values of the measured temperatures is linked to the power loss in the cables and eventually other stray losses, which are not accounted for in the simulations.

4.4 | Cross-coupling in array configurations

The mutual coupling between the two adjacent antennas placed on top of a flat phantom is presented by the dotted lines in Figure 7. This setup, with antennas placed in vicinity of each other, presents the interleaved antenna placement in an array configuration. In general, there is a reasonable agreement

between the simulated and measured results, with a maximum coupling of -25 dB in the simulated and -35 dB in the measured cases.

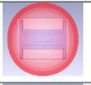

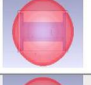
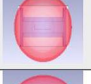


In phased array applications, the coupling between antennas depends on the geometry and thus a different loading effect of the body. Therefore, a scenario with a cylindrical muscle phantom, placed in the centre of the applicator according to Figure 6a, was considered. Figure 17 demonstrates that the level of crosstalk among the elements is better than -20 dB throughout the frequency band, which is promising and good news also for sensing applications such as MW thermometry (MWT) [26].

4.5 | Power deposition capability

The capability of the antenna to deposit EM energy into a large, deep-seated, intracranial tumour is exemplified in

Figure 18. A hybrid PSO-based beamforming technique [45] was used to find the coefficients of the antennas at 400 MHz for a simultaneous excitation. Figure 18a, 18b and 18c show the achieved power loss density distributions in the transverse, coronal, and sagittal planes, respectively. The tumour border is outlined by the solid black line in these figures. Note that the hotspots emerging on the skin will not be treatment-limiting or problematic here because they are cooled down by the water bolus. A visual

TABLE 2 Effective field size (EFS) and penetration depth of the design at several frequency samples within the band.

Frequency (MHz)	SAR _{Max1cm} (W/Kg)	EPD (mm)	EFS
400	56.7	9.71	
500	55.5	9.41	
600	57.02	10.17	
650	57.33	8.99	
700	53.16	8.99	
800	29.74	7.7	

Abbreviations: EPD, effective penetration depth; EFS, effective field size; SAR, specific absorption rate.

inspection of this application example indicates the suitability of the proposed antenna for deep HT in challenging cancer sites.

4.6 | Overall comparison

Table 3 provides a summary of the ORWG characteristics and contrasts them with the state-of-the-art designs in the field. The aspects in which ORWG performs better are highlighted in bold. The ORWG antenna exhibits the widest bandwidth with aperture dimensions smaller than most other designs. Along with having effective radiation characteristics, as demonstrated above, the ORWG becomes an attractive design for use as a single HT applicator or an element in phased array applicators. Compatibility with the MR bore may be a potential limitation for a modern deep applicator utilising the ORWG antenna. This parameter remains to be investigated while other designs such as SGBW or Yagi-Uda antennas have already been proven suitable for the dual operation of thermal intervention and monitoring.

Note that Table 3 contains only the models specifically tailored for HT and does not include antennas designed for other biomedical applications such as MW imaging (MWI). Despite similarities in near-field operations, the requirements for HT antennas are slightly different from the designs proposed for MWI or on-body applications; HT antennas operate at high powers of typically 150 W, requiring a water bolus to be placed between the patient and antenna. Moreover, HT antennas are mainly designed for the UHF band, which is lower than the most common bands utilised for diagnostic purposes.

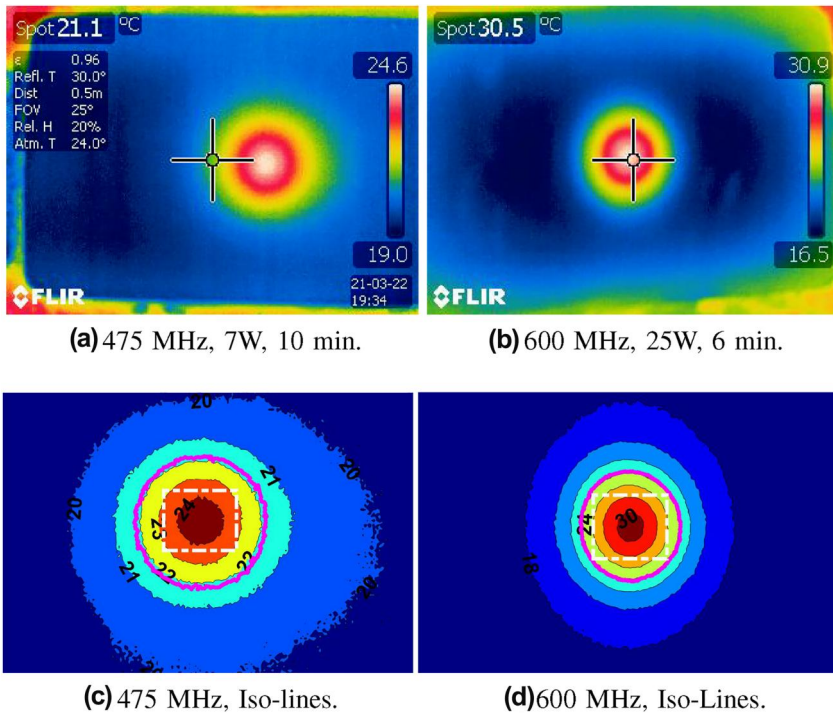


FIGURE 15 Temperature profile 1 cm below the surface of the muscle phantom captured using an IR-camera for (a) input power of 7 W fed to the antenna for 10 min at 475 MHz and (b) input power of 25 W fed to the antenna for 6 min at 600 MHz. (c) and (d) are the corresponding iso-lines of the temperature profiles (the aperture of the antenna and 50% iso-line are also shown as the dashed white and solid magenta lines, respectively)

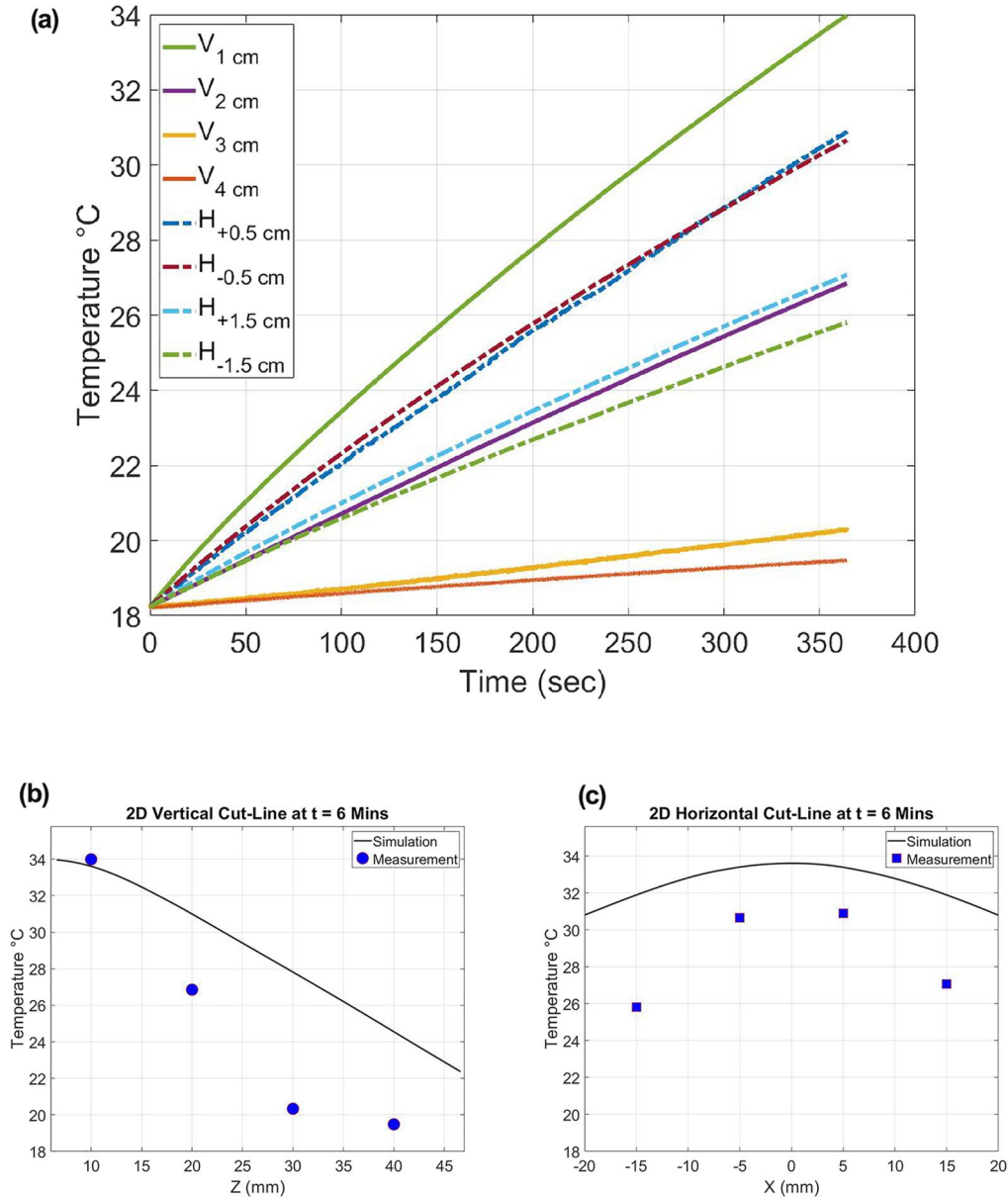


FIGURE 16 Fibre optic probes measurement. (a) Rate of temperature change recorded using the probes within 6 min of exposure at 600 MHz (solid lines are for the vertical probes). (b) and (c) show the comparison between the measured and simulated temperature at the last time step across the vertical and horizontal lines, respectively

5 | CONCLUSION

Performance assessments in this study show that the proposed ORWG antenna has high potential to serve not only as an element in a phased array applicator but also as an applicator for superficial HT. In particular, it offers a directive radiation pattern, has a UWB impedance bandwidth, and needs no RF matching circuits. The measured reflection coefficient of the design is below -10 dB from 367 up to 820 MHz (75.5% fractional bandwidth). The antenna further exhibits low susceptibility to environmental noise and mutual coupling, as an inherent attribute of waveguide type antennas. The sensitivity analysis proves the robustness of the design against local variations of

inhomogeneous tissue-loading and the water bolus thickness. The efficacy of the fabricated antenna was validated through the metrics recommended by the ESHO. Measurement results are in good agreement with the simulations. The EFS is greater than the physical dimension of the 3×4 cm aperture. The mutual coupling between two adjacent elements in the array is lower than -30 dB throughout the entire band while measured in a flat phantom arrangement. In summary, the performance assessments show that the ORWG antenna has a high potential to serve as an element in HT-phased arrays as illustrated by an excellent focus achieved in a large brain tumour in a realistic patient model. The utilisation of the proposed design may also extend beyond HT to other biomedical applications.

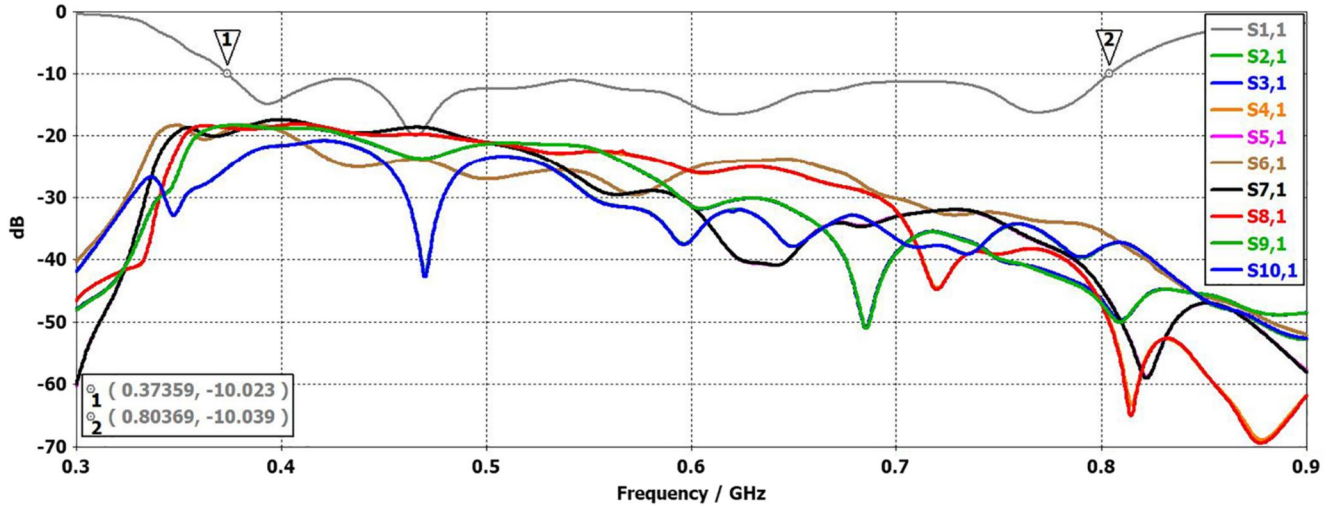


FIGURE 17 Mutual coupling among the 10 elements of the cylindrical array

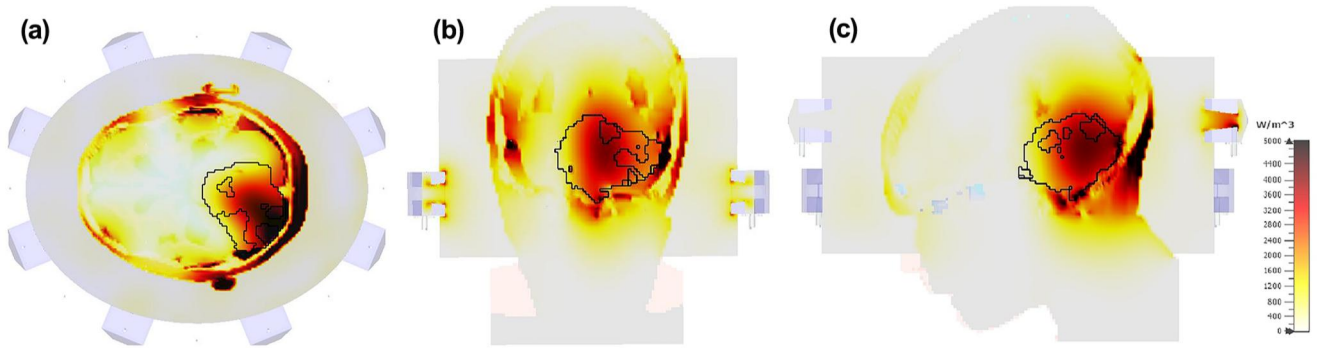


FIGURE 18 Application of Open Ridged-Waveguide (ORWG) in a hyperthermia (HT) elliptical array for childhood cancer therapy. (a), (b), and (c) are power loss density (PLD) distributions in transverse, coronal, and sagittal planes, respectively. The outline of the tumour is shown in a solid black line

TABLE 3 Comparison of Open Ridged-Waveguide (ORWG) with some of the models proposed in the literature for hyperthermia (HT) applicators

Characteristic	Waveguide [16, 17]	Dipole [15]	Patch [18, 19]	Bow-tie [20]	Yagi-Uda [49, 50]	SGBW [21]	ORWG
Bandwidth [MHz] $S_{11} \leq -10\text{dB}$	≤ 10 [65–75]	50 [70–120]	$\cong 40$ [415–450]	143 [226–369]	$\cong 60$ [400–462]	$\cong 400$ [430–800]	$\cong 450$ [367–820]
High to low frequency ratio	1:1.15	1:1.71	1:1.08	1:1.63	1:1.16	1:1.86	1:2.23
Radiation pattern	Directional	Omni-directional	Semi-directional	Directional	Directional	Directional	Directional
Matching circuit	No	Yes	No	Yes	No	Yes	No
Dimension [mm]	Aperture 80 × 340	Length 30.75	27.8 × 10	156 × 70	65 × 50	60 × 60	30 × 40
MR compatibility	-	Yes	Yes	Yes	Yes	Yes	To be investigated

Note: The bold entries show where the performance of new design surpasses its predecessors.

Abbreviations: ORWG, Open Ridged-Waveguide; SGBW, self-grounded bow-tie.

ACKNOWLEDGEMENT

The authors would like to thank Dr. Karan Gumber for his help and assistance in the lab during the experiments.

CONFLICT OF INTEREST

There is no conflict of interest.

PERMISSION TO REPRODUCE MATERIALS FROM OTHER SOURCES

None.

DATA AVAILABILITY STATEMENT

Data available on request from the authors.

ORCID

Morteza Ghaderi Aram  <https://orcid.org/0000-0003-2073-6966>

REFERENCES

- Overgaard, J., et al.: Randomised trial of hyperthermia as adjuvant to radiotherapy for recurrent or metastatic malignant melanoma. *Lancet*. 345(8949), 540–543 (1995)
- van der Zee, J., et al.: Dutch deep hyperthermia group. comparison of radiotherapy alone with radiotherapy plus hyperthermia in locally advanced pelvic tumours: a prospective, randomised, multicentre trial. *Lancet*. 355(9210), 1119–1125 (2000)
- Datta, N.R., et al.: Hyperthermia and radiotherapy in the management of head and neck cancers: a systematic review and meta-analysis. *International Journal of Hyperthermia*. 32(1), 31–40 (2016)
- Liem, E.I., et al.: Chemohyperthermia in non-muscle-invasive bladder cancer: an overview of the literature and recommendations. *International Journal of Hyperthermia*. 32(4), 363–373 (2016)
- Issels, R.D., et al.: Effect of neoadjuvant chemotherapy plus regional hyperthermia on long-term outcomes among patients with localized high-risk soft tissue sarcoma: the EORTC 62961-ESHO 95 randomized clinical trial. *JAMA Oncol*. 4(4), 483–492 (2018)
- Paulides, M., et al.: Recent technological advancements in radiofrequency-and microwave-mediated hyperthermia for enhancing drug delivery. *Adv. Drug Deliv. Rev.* 163, 3–18 (2020)
- Takook, P., Persson, M., Trefná, H.D.: Performance evaluation of hyperthermia applicators to heat deep-seated brain tumors. *IEEE J. of Electromagn., RF and Microw. in Med. Biol.* 2(1), 18–24 (2018)
- Schooneveldt, G., et al.: Hyperthermia treatment planning including convective flow in cerebrospinal fluid for brain tumour hyperthermia treatment using a novel dedicated paediatric brain applicator. *Cancers*. 11(8), 1183 (2019)
- Van der Gaag, M., et al.: Development of a guideline for the water bolus temperature in superficial hyperthermia. *Int. J. Hyperther.* 22(8), 637–656 (2006)
- Arunachalam, K., et al.: Design of a water coupling bolus with improved flow distribution for multi-element superficial hyperthermia applicators. *Int. J. Hyperther.* 25(7), 554–565 (2009)
- Lee, J., Nam, S.: Effective area of a receiving antenna in a lossy medium. *IEEE Trans. Antenn. Propag.* 57(6), 1843–1845 (2009)
- Aguilar, S.M., et al.: Multiband miniaturized patch antennas for a compact, shielded microwave breast imaging array. *IEEE Trans. Antenn. Propag.* 62(3), 1221–1231 (2013)
- Trefná, H.D., et al.: Quality assurance guidelines for superficial hyperthermia clinical trials. *Strahlenther. Onkol.* 193(5), 351–366 (2017)
- Trefná, H.D., et al.: Quality assurance guidelines for superficial hyperthermia clinical trials: I. clinical requirements. *Int. J. Hyperther.* 33(4), 471–482 (2017)
- Turner, P., Tumeah, A., Schaefermeyer, T.: BSD-2000 approach for deep local and regional hyperthermia: physics and technology. *Strahlenther. Onkol.: Organ der Deutschen Röntgengesellschaft...[et al.]*. 165(10), 738–741 (1989)
- Crezee, J., et al.: Improving locoregional hyperthermia delivery using the 3-D controlled AMC-8 phased array hyperthermia system: a preclinical study. *Int. J. Hyperther.* 25(7), 581–592 (2009)
- Zweije, R., et al.: Technical and clinical evaluation of the ALBA-4D 70MHz loco-regional hyperthermia system. In: 2018 48th European Microwave Conference (EuMC), pp. 328–331. IEEE (2018)
- Paulides, M.M., et al.: A patch antenna design for application in a phased-array head and neck hyperthermia applicator. *IEEE (Inst. Electr. Electron. Eng.) Trans. Biomed. Eng.* 54(11), 2057–2063 (2007)
- Paulides, M., et al.: The HYPERcollar: a novel applicator for hyperthermia in the head and neck. *Int. J. Hyperther.* 23(7), 567–576 (2007)
- Winter, L., et al.: Design and evaluation of a hybrid radiofrequency applicator for magnetic resonance imaging and RF induced hyperthermia: electromagnetic field simulations up to 14.0 Tesla and proof-of-concept at 7.0 Tesla. *PLoS One*. 8(4), e61661 (2013)
- Takook, P., et al.: Compact self-grounded bow-tie antenna design for an UWB phased-array hyperthermia applicator. *Int. J. Hyperther.* 33(4), 387–400 (2017)
- Eigentler, T.W., et al.: Wideband self-grounded bow-tie antenna for thermal mr. *NMR Biomed.* 33(5), e4274 (2020)
- Oberacker, E., et al.: Radiofrequency applicator concepts for thermal magnetic resonance of brain tumors at 297 MHz (7.0 Tesla). *Int. J. Hyperther.* 37(1), 549–563 (2020)
- Kazempour, A., Begaud, X.: Calculable dipole antenna for EMC measurements with low-loss wide-band balun from 30 MHz to 2 GHz. *Electromagnetics*. 25(3), 187–202 (2005)
- Wust, P., et al.: Antenna arrays in the SIGMA-eye applicator: interactions and transforming networks. *Med. Phys.* 28(8), 1793–1805 (2001)
- Aram, M.G., Beilina, L., Trefna, H.D.: Microwave thermometry with potential application in non-invasive monitoring of hyperthermia. *J. Inverse Ill-Posed Probl.* 1 (2020)
- Van Rhooon, G., Rietveld, P., Van der Zee, J.: A 433 MHz lucite cone waveguide applicator for superficial hyperthermia. *Int. J. Hyperther.* 14(1), 13–27 (1998)
- Abbas-Azimi, M., Arazm, F., Faraji-Dana, R.: Design and optimisation of a high-frequency EMC wideband horn antenna. *IET Microw. Antenn. Propag.* 1(3), 580–585 (2007)
- Mehrdadian, A., et al.: Design and implementation of 0.7 to 7 GHz broadband double-ridged horn antenna. In: 7th International Symposium on Telecommunications (IST'2014), pp. 250–255. IEEE (2014)
- Jacobs, B., Odendaal, J., Joubert, J.: Modelling manufacturing tolerances in 1–18 GHz double-ridged horn antennas. In: 2009 European Microwave Conference (EuMC), pp. 1484–1487. IEEE (2009)
- Cohn, S.B.: Properties of ridge wave guide. *PIRE*. 35(8), 783–788 (1947)
- Hopfer, S.: The design of ridged waveguides. *IRE Trans. Microw. Theory Tech.* 3(5), 20–29 (1955)
- Sun, W., Balanis, C.A.: MFIE analysis and design of ridged waveguides. *IEEE Trans. Microw. Theor. Tech.* 41(11), 1965–1971 (1993)
- Venkatesan, V., Selvan, K.T.: Rigorous gain measurements on wide-band ridge horn. *IEEE Trans. Electromagn. C.* 48(3), 592–594 (2006)
- Hoefler, W.J., Burton, M.N.: Closed-form expressions for the parameters of finned and ridged waveguides. *IEEE Trans. Microw. Theor. Tech.* 30(12), 2190–2194 (1982)
- Mallahzadeh, A.R., Imani, A.: Double-ridged antenna for wideband applications. *Prog. Electromagn. Res.* 91, 273–285 (2009)
- Lee, R.T., Smith, G.S.: A design study for the basic TEM horn antenna. *IEEE Antenn. Propag. Mag.* 46(1), 86–92 (2004)
- Latif, S., et al.: Parametric study of a water-filled double-ridged horn antenna for biomedical imaging application. In: 2012 15 International Symposium on Antenna Technology and Applied Electromagnetics, pp. 1–2. IEEE (2012)
- Lee, E.: Electromagnetic superficial heating technology. In: *Thermoradiotherapy and thermochemotherapy*, pp. 193–217. Springer (1995)

40. CST: Cst microwave studio advanced topics (Technical Report). CST-Computer Simulation Technology (2019)
41. Gabriel, C.: Compilation of the dielectric properties of body tissues at RF and microwave frequencies (Technical Report). King's College London (United Kingdom) Department of Physics (1996)
42. Trefná, H.D., Ström, A.: Hydrogels as a water bolus during hyperthermia treatment. *Phys. Med. Biol.* 64(11), 115025 (2019)
43. Amineh, K.R., Trehan, A., Nikolova, N.K.: TEM horn antenna for ultra-wide band microwave breast imaging. *Prog. Electromagn. Res.* 13, 59–74 (2009)
44. Hand, J.W., et al.: *Methods of external hyperthermic heating*. Springer Science & Business Media (2012)
45. Aram, M.G., Aliakbarian, H., Trefná, H.D.: A phased array applicator based on open ridged-waveguide antenna for microwave hyperthermia. *Microw. Opt. Technol. Lett.* 63(12), 3086–3091 (2021)
46. Canters, R., et al.: A literature survey on indicators for characterisation and optimisation of SAR distributions in deep hyperthermia, a plea for standardisation. *Int. J. Hyperther.* 25(7), 593–608 (2009)
47. Amineh, R.K., et al.: Near-field microwave imaging based on aperture raster scanning with TEM horn antennas. *IEEE Trans. Antenn. Propag.* 59(3), 928–940 (2010)
48. Diana, S., et al.: A compact double ridged horn antenna for ultra-wide band microwave imaging. *IEEE Open J. Antennas Propag.* (2021)
49. Paulides, M., et al.: A printed Yagi–Uda antenna for application in magnetic resonance thermometry guided microwave hyperthermia applicators. *Phys. Med. Biol.* 62(5), 1831–1847 (2017)
50. Drizdal, T., et al.: Simulation guided design of the MRcollar: a MR compatible applicator for deep heating in the head and neck region. *Int. J. Hyperther.* 38(1), 382–392 (2021)

How to cite this article: Ghaderi Aram, M., Aliakbarian, H., Dobšiček Trefná, H.: An ultra-wideband compact design for hyperthermia: Open ridged-waveguide antenna. *IET Microw. Antennas Propag.* 1–16 (2022). <https://doi.org/10.1049/mia2.12226>